ARTICLE

Revealing excited states of rotational Bose-Einstein condensates

Jianyuan Yin,[1,2] Zhen Huang,[3] Yongyong Cai,[4] Qiang Du,[5] and Lei Zhang[6,*]

*Correspondence: zhangl@math.pku.edu.cn

Received: June 20, 2023; Accepted: November 20, 2023; Published Online: November 23, 2023; https://doi.org/10.1016/j.xinn.2023.100546

GRAPHICAL ABSTRACT

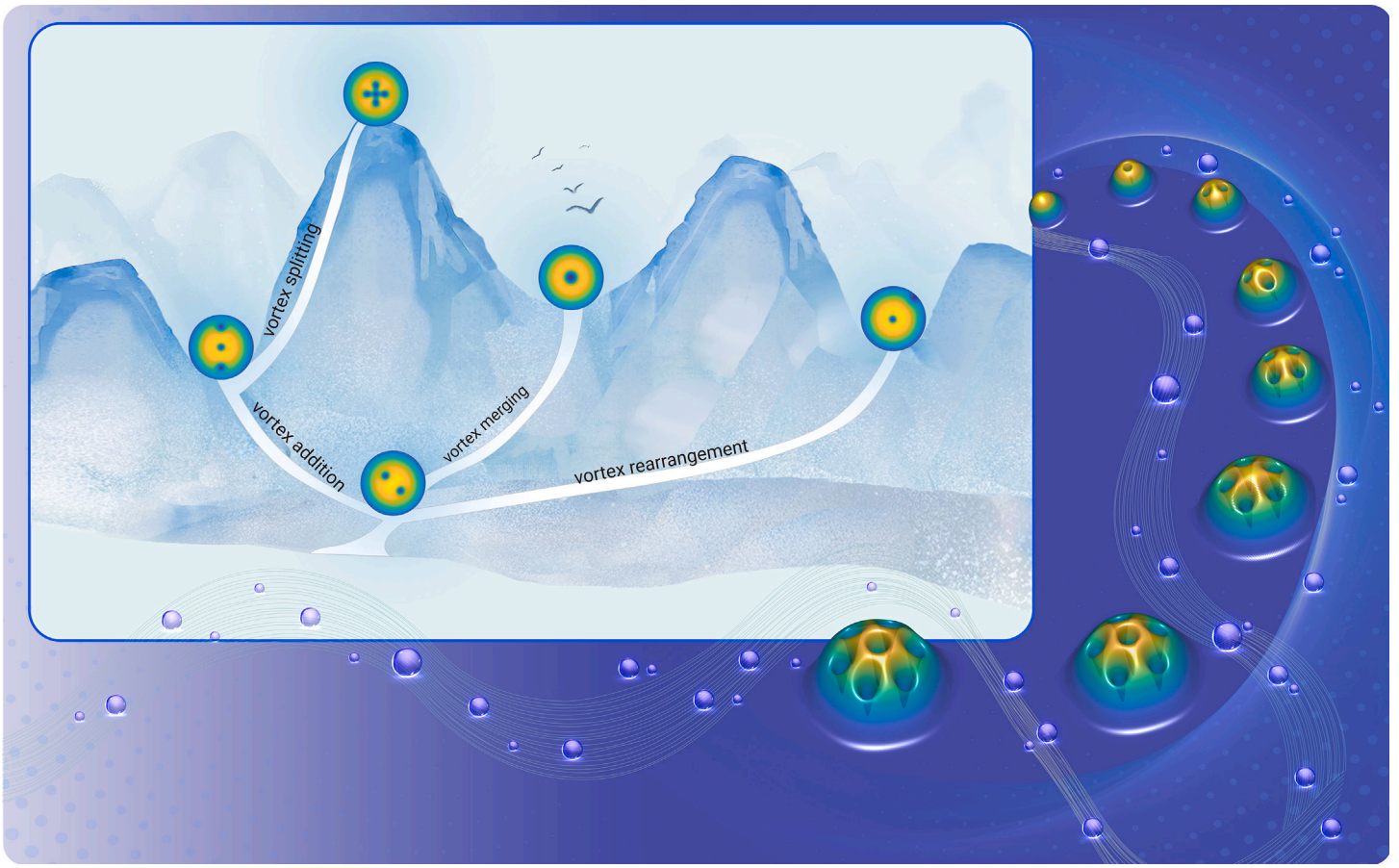

PUBLIC SUMMARY

- Solution landscapes of rotational Bose-Einstein condensates are constructed to reveal ground and excited states.
- Four excitation mechanisms are identified: vortex addition, rearrangement, merging, and splitting.
- Evolution of the stability of different ground states is deciphered.

ARTICLE

Revealing excited states of rotational Bose-Einstein condensates

Jianyuan Yin,[1,2] Zhen Huang,[3] Yongyong Cai,[4] Qiang Du,[5] and Lei Zhang[6,*]

[1]School of Mathematical Sciences, Laboratory of Mathematics and Applied Mathematics, Peking University, Beijing 100871, China
[2]Department of Mathematics, National University of Singapore, Singapore 119076, Singapore
[3]Department of Mathematics, University of California, Berkeley, Berkeley, CA 94720, USA
[4]School of Mathematical Sciences, Beijing Normal University, Beijing 100875, China
[5]Department of Applied Physics and Applied Mathematics and Data Science Institute, Columbia University, New York, NY 10027, USA
[6]Beijing International Center for Mathematical Research, Center for Quantitative Biology, Center for Machine Learning Research, Peking University, Beijing 100871, China
*Correspondence: zhangl@math.pku.edu.cn

Received: June 20, 2023; Accepted: November 20, 2023; Published Online: November 23, 2023; https://doi.org/10.1016/j.xinn.2023.100546

Citation: Yin J., Huang Z., Cai Y., et al., (2023). Revealing excited states of rotational Bose-Einstein condensates. The Innovation **5(1)**, 100546.

Rotational Bose-Einstein condensates can exhibit quantized vortices as topological excitations. In this study, the ground and excited states of the rotational Bose-Einstein condensates are systematically studied by calculating the stationary points of the Gross-Pitaevskii energy functional. Various excited states and their connections at different rotational frequencies are revealed in solution landscapes constructed with the constrained high-index saddle dynamics method. Four excitation mechanisms are identified: vortex addition, rearrangement, merging, and splitting. We demonstrate changes in the ground state with increasing rotational frequencies and decipher the evolution of the stability of ground states.

INTRODUCTION

Quantized vortices as topological defects play a crucial role in the study of superfluidity and superconductivity.[1,2] These vortices have been the subject of extensive research in Bose-Einstein condensates (BECs) of degenerate quantum gases, both theoretically and experimentally.[3–6] A common scenario for generating these topological defects is when the system is stirred by rotating laser beams.[7–11] As the rotational frequency increases, the vortex structures experience successive complex topological changes.[12–14]

Theoretically, the problem of identifying stationary vortex states of rotational BECs can be effectively solved by finding the stationary points of the Gross-Pitaevskii (G-P) energy functional with an equality constraint corresponding to the mass conservation.[6] The local nature of a stationary point is often described by its (Morse) index in Morse theory[15] (i.e., the number of negative eigenvalues of the Hessian). For example, a local minimizer has an index zero and can be computed using the imaginary time integration of the dynamic G-P equation. A stationary state with a nonzero index would be a saddle point due to its unstable nature. The global minimizer is often referred to as the ground state. Stationary points with higher values of energy, consisting of both local minimizers and saddle points, are called excited states.

Contrary to many computational efforts for finding ground states,[16–23] there are no controllable search algorithms to systematically explore energy landscapes and compute excited states. From well-chosen initial guesses, some excited states with certain symmetry can be obtained using Newton's methods,[24,25] or deflated continuation algorithms.[26] The observations of vortex nucleation in BECs have been reported in many publications,[27–29] which characterize transitions between ground states and metastable vortex states. However, a global landscape of excited states of BECs remains largely unexplored. Excitation mechanisms between different vortex states, which provide the dynamical pathway from a ground/excited state to another, are still a mystery.

In this article, we systematically examine excited states and excitation mechanisms of two-dimensional (2D) BECs trapped in an isotropic harmonic-oscillator potential within the framework of mean-field theory, assuming that no excitations are caused along the z axis. Specifically, we apply an efficient numerical method based on the constrained high-index saddle dynamics (CHiSD) to construct the solution landscape of the G-P energy. The solution landscape is a pathway map consisting of all of the stationary points and their connections,[30,31] which provides an efficient approach to finding multiple stationary points and their connections without tuning random initial guesses. This methodology has been successfully applied to liquid crystals,[32–35] quasicrystals,[36] and diblock copolymers.[37] Using the solution landscape approach, we reveal four excitation mechanisms of BECs: vortex addition, rearrangement, merging, and splitting. We further demonstrate how the ground state changes with increasing rotational frequencies and the evolution of the stability of the ground states.

MODELS AND METHODS

G-P energy

A stationary vortex state of 2D rotational BECs can be characterized as a stationary point of the G-P energy (a dimensionless form),[6]

$$E(\phi)=\int\left\{\frac{1}{2}|\nabla\phi|^2+V|\phi|^2+\frac{\beta}{2}|\phi|^4-\Omega\overline{\phi}L_z\phi\right\}\mathrm{d}\boldsymbol{x}, \qquad \text{(Equation 1)}$$

on the unit sphere $\phi\in\mathcal{M}=\{\varphi\in L^2(\mathbb{R}^2,\mathbb{C}):E(\varphi)<\infty,\int|\varphi|^2\mathrm{d}\boldsymbol{x}=1\}$. Here, ϕ is the complex-valued wave function of BECs defined on $\mathbb{R}^2$ and $|\phi|^2$ represents the particle density. $V(\boldsymbol{x})$ is the trapping potential and β characterizes the interaction rate. Ω is the rotational frequency and $L_z=-\mathrm{i}(x\partial_y-y\partial_x)$ is the z component of the angular momentum operator. Equivalently, each stationary point solves a nonlinear eigenvalue problem,

$$\mu\phi=\left(-\frac{1}{2}\nabla^2+V+\beta|\phi|^2-\Omega L_z\right)\phi, \qquad \text{(Equation 2)}$$

where μ is the chemical potential calculated as

$$\mu=\int\left\{\frac{1}{2}|\nabla\phi|^2+V|\phi|^2+\beta|\phi|^4-\Omega\overline{\phi}L_z\phi\right\}\mathrm{d}\boldsymbol{x}, \qquad \text{(Equation 3)}$$

or equivalently,

$$\mu=E(\phi)+\int\frac{\beta}{2}|\phi|^4\mathrm{d}\boldsymbol{x}. \qquad \text{(Equation 4)}$$

In our numerical experiments, V is taken as an isotropic harmonic oscillator $V(\boldsymbol{x})=\frac{1}{2}|\boldsymbol{x}|^2$. A strongly repulsive interaction regime is considered to be $\beta=300$. The physical units of parameters in this dimensionless model are well documented in the references.[6,12]

The (Riemannian) gradient of the G-P energy (Equation 1) is written as

$$\begin{aligned}\mathrm{grad}E(\phi)&=\mathcal{P}_\phi\nabla E(\phi)=2\mathcal{P}_\phi\left(\frac{\delta E}{\delta\overline{\phi}}\right)\\&=\mathcal{P}_\phi\left(-\nabla^2\phi+2V\phi+2\beta|\phi|^2\phi-2\Omega L_z\phi\right).\end{aligned} \qquad \text{(Equation 5)}$$

Here, $\mathcal{P}_\phi$ is the projection operator on the tangent space $T(\phi)=\{\psi:\langle\psi,\phi\rangle=0\}$, defined as,

$$\mathcal{P}_\phi\psi=\psi-\langle\psi,\phi\rangle\phi. \qquad \text{(Equation 6)}$$

The inner product is defined as

$$\langle\psi,\phi\rangle=\phi^\top\psi=\mathrm{Re}\left(\int\overline{\phi}\psi\mathrm{d}\boldsymbol{x}\right). \qquad \text{(Equation 7)}$$

$\widehat{\phi}\in\mathcal{M}$ is a stationary state of BECs if the gradient vanishes (i.e., $\mathrm{grad}E(\widehat{\phi})=0$), which is equivalent to the nonlinear eigenvalue problem in (Equation 2).

The (Riemannian) Hessian is, for $\nu\in T(\phi)$,

$$\begin{aligned}\mathrm{Hess}E(\phi)[v] &= \mathcal{P}_\phi(\partial_v \mathrm{grad}E(\phi))\\ &= \mathcal{P}_\phi\left(\nabla^2 E(\phi)v\right) - \langle \phi, \nabla E(\phi)\rangle v.\end{aligned} \tag{Equation 8}$$

The Hessian can be extended to the whole space as a self-adjoint operator $\mathrm{Hess}E(\phi)[\mathcal{P}_\phi v]$. In numerical computation, we use central difference schemes to approximate spatial derivatives of ϕ in Equations 5 and 8.

The index of a stationary state $\widehat{\phi} \in \mathcal{M}$ is calculated as the number of negative eigenvalues of the Hessian $\mathrm{Hess}E(\widehat{\phi})$. Methods for partial eigenvalue problems, such as the locally optimal block preconditioned conjugate gradient method,[38] can be applied to calculate the index and corresponding eigenfunctions within a small computational cost.

Some invariance properties exist in the G-P energy. From the radial symmetry of the isotropic trapping potential $V(\boldsymbol{x})$, for a stationary state $\widehat{\phi} \in \mathcal{M}$ and any $\vartheta \in \mathbb{R}$, a global phase translation $e^{i\vartheta}\widehat{\phi}$ and a rotation around the origin $\widehat{\phi}(x\cos\vartheta - y\sin\vartheta, x\sin\vartheta + y\cos\vartheta)$ are also stationary states with the same index and energy. This property indicates that, in general, the Hessian at a stationary state has two zero eigenvalues. As a special case, the states with one central vortex of a winding number m or no vortex ($m = 0$) can be expressed as $e^{im\theta}\varphi_m(r)$ in polar coordinates (r, θ), so the Hessians at these stationary points have only one zero eigenvalue.[6,13] Different multiplicities of zero eigenvalues would pose some difficulties in numerical computations. For some stationary states, Hessians have more zero eigenvalues, as explained in the supplemental information, and consequently we obtain multiple numerical results of some states as shown in Figure S1.

CHiSD method

Here, we briefly introduce the CHiSD method and its numerical implementations to calculate the excited states, and the details can be found in reference [39]. The CHiSD method can be regarded as a generalization of the imaginary time method to compute an index-k saddle point (k-saddle). For the sphere constraint, the CHiSD for a k-saddle (k-CHiSD) is

$$\begin{cases}\dot{\phi} = -\left(\boldsymbol{I} - \sum_{i=1}^{k} 2v_i v_i^\top\right)\mathrm{grad}E(\phi),\\ \dot{v}_i = -\left(\boldsymbol{I} - v_i v_i^\top - \sum_{j=1}^{i-1} 2v_j v_j^\top\right)\mathrm{Hess}E(\phi)[v_i]\\ \qquad\quad - \langle v_i, \mathrm{grad}E(\phi)\rangle\phi, \qquad i = 1, \cdots, k,\end{cases} \tag{Equation 9}$$

coupled with an initial condition satisfying

$$\phi \in \mathcal{M}, \quad \langle \phi, v_i\rangle = 0, \quad \langle v_i, v_j\rangle = \delta_{ij}. \tag{Equation 10}$$

We refer to some references ([39,40]) for CHiSD methods for general constraints and the numerical analysis, respectively.

With an initial condition satisfying Equation 10, the k-CHiSD of Equation 9 always satisfies the constraints in Equation 10. The dynamics of ϕ in Equation 9 represents a transformed gradient flow on $\mathcal{M}$, which consists of the gradient ascent along the tangent directions of $v_1, \cdots, v_k$, and the gradient descent along other orthogonal tangent directions. Therefore, the dynamics attempts to maximize the energy only on a k-dimensional submanifold. Meanwhile, the dynamics of v_i in Equation 9 finds the normalized eigenvector corresponding to the i-th smallest eigenvalue of $\mathrm{Hess}E(\phi)$.

To ensure these constraints in numerical implementations, we use the numerical tools of retractions and vector transport in manifold optimization.[41] A retraction R_ϕ moves $\phi \in \mathcal{M}$ along a tangent vector $\eta_\phi \in T(\phi)$ on the manifold to $R_\phi(\eta_\phi)$. When ϕ moves on $\mathcal{M}$ along a tangent vector $\eta_\phi \in T(\phi)$ characterized as $R_\phi(\eta_\phi)$, the vector transport $\mathcal{T}_{\eta_\phi}(v_\phi)$ gives how to numerically change a tangent vector $v_\phi \in T(\phi)$ to a tangent vector at $R_\phi(\eta_\phi)$ accordingly, as a generalization of parallel translation. There is a considerable amount of flexibility in how to choose the retraction and vector transport, whereas different choices may lead to different results. In our numerical computations, we apply a retraction operator of

$$R_\phi(\eta_\phi) = \frac{\phi + \eta_\phi}{\|\phi + \eta_\phi\|}, \tag{Equation 11}$$

and a vector transport of

$$\mathcal{T}_{\eta_\phi} v_\phi = v_\phi - \frac{\langle v_\phi, \phi + \eta_\phi\rangle}{\|\phi + \eta_\phi\|^2}(\phi + \eta_\phi). \tag{Equation 12}$$

With the retraction operator R and the vector transport $\mathcal{T}$, the k-CHiSD in Equation 9 can be numerically implemented with the initial condition satisfying Equation 10. We aim to calculate $\phi^{(n+1)}$ and $v_i^{(n+1)}$ at the $(n+1)$-th iteration step based on $\phi^{(n)}$ and $v_i^{(n)}$ in the previous step. For the dynamics of ϕ, we can implement an explicit scheme with a retraction as

$$\begin{aligned}\phi^{(n+1)} &= R_{\phi^{(n)}}\left(\alpha^{(n)}\eta^{(n)}\right),\\ \eta^{(n)} &= -\left(\boldsymbol{I} - \sum_{i=1}^{k} 2v_i^{(n)} v_i^{(n)\top}\right)\mathrm{grad}E\left(\phi^{(n)}\right),\end{aligned} \tag{Equation 13}$$

to calculate $\phi^{(n+1)}$ with a step size $\alpha^{(n)}$. Note that $v_1^{(n)}, \cdots, v_k^{(n)}$ are orthonormal vectors in $T(\phi^{(n)})$, so $\eta^{(n)}$ lies in the tangent space $T(\phi^{(n)})$, and then ϕ remains in the manifold $\mathcal{M}$ due to retraction. Then, the vector transport $\mathcal{T}_{\alpha^{(n)}\eta^{(n)}}$ at $\phi^{(n)}$ moves $\{v_i^{(n)}\}$ to $\{\tilde{v}_i^{(n)}\}$ in the tangent space $T(\phi^{(n+1)})$, which is characterized by the second term in v_i dynamics. The first term in v_i dynamics aims to solve an eigenvalue problem:

$$\begin{aligned}&\min_{v_i}\left\langle \mathrm{Hess}E\left(\phi^{(n+1)}\right)\left[\mathcal{P}_{\phi^{(n+1)}} v_i\right], v_i\right\rangle\\ &\text{s.t.}\ \left\langle \phi^{(n+1)}, v_i\right\rangle = 0, \quad \langle v_j, v_i\rangle = \delta_{ij}, j = 1, \cdots, i,\end{aligned} \tag{Equation 14}$$

using gradient flow. Because the transported vector $\tilde{v}_i^{(n)}$ provides a good initial guess for this problem, we can apply one-step gradient descent to solve this in each iteration. Generally speaking, vector transport may not maintain the orthonormality, so a Gram-Schmidt procedure is finally implemented in the obtained vectors. The iteration is terminated if $\left\|\mathrm{grad}E(\phi^{(n)})\right\|$ is smaller than tolerance.

In numerical computations, the wave function ϕ is truncated into a bounded domain $D = [-8, 8]^2$ with homogeneous Dirichlet boundary conditions on ∂D because stationary states decay to zero exponentially in the far field due to the effect of the trapping potential $V(\boldsymbol{x})$.[6] The wave function ϕ is discretized using finite difference methods with $N = 128$ nodes along each dimension.

Downward and upward search algorithms

To identify excited states and excitation mechanisms, we combine the CHiSD method with the following downward search algorithm to construct the solution landscape.[30,31]

From an index-k saddle point ϕ^* with orthonormal eigenvectors $v_1^*, \cdots, v_k^* \in T(\phi^*)$ corresponding to the negative eigenvalues of $\mathrm{Hess}E(\phi^*)$, we choose an unstable direction v_i^* from them as the perturbation direction. Then, an m-CHiSD ($m < k$) is simulated from $R_{\phi^*}(\varepsilon v_i^*)$ with the initial directions $\{\mathcal{T}_{\varepsilon v_i^*} v_1, \cdots, \mathcal{T}_{\varepsilon v_i^*} v_m\}$, where $v_1, \cdots, v_m$ are chosen from the other unstable eigenvectors $\{v_1^*, \cdots, v_{i-1}^*, v_{i+1}^*, \cdots, v_k^*\}$. Here, a small constant ε, positive or negative, pushes the system away from the saddle point. An orthogonal normalization procedure could be applied to the initial directions before simulation. Different choices of m, v_i^*, and the sign of ε may lead to different states. By repeating this algorithm to newly found states, we can finally reach different excited states and obtain connection relationships between states. For the illustration example in Figure 1, from the index-2 stationary point A, two unstable directions lead to different 1-saddles B_1 and B_2 using 1-CHiSD. Then, the minimizer C is obtained from either B_1 or B_2 by 0-CHiSD (i.e., gradient dynamics).

The downward search algorithm enables us to find multiple excited states from a high-index excited state. However, we can also apply an upward search algorithm to find high-index excited states starting from a low-index excited state or a ground state, when the high-index excited state is unknown or multiple high-index excited states exist.[30] Given an index-k saddle point $\phi^\star$ with l zero eigenvalues, we calculate the orthonormal eigenvectors $v_1^\star, \cdots, v_m^\star \in T(\phi^\star)$ corresponding to the smallest m eigenvalues $\lambda_1^\star \leqslant \cdots \leqslant \lambda_m^\star$ of $\mathrm{Hess}E(\phi^\star)$, where $m > k + l$ so that $\lambda_m^\star > 0$. Then, an m-CHiSD ($m > k$) is numerically simulated from $R_{\phi^\star}(\varepsilon v_m^\star)$, and the initial directions are reorthonormalization of $\mathcal{T}_{\varepsilon v_m^\star} v_1^\star$, $\cdots$, $\mathcal{T}_{\varepsilon v_m^\star} v_m^\star$. Here, ε is also a small constant that could be positive or negative. This algorithm can also be repeated to newly found states. In the illustration

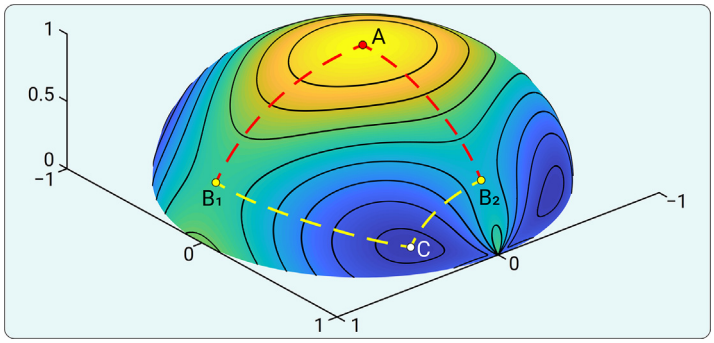

Figure 1. Illustration of the solution landscape on a unit sphere Two 1-saddles, B_1 and B_2, are connected to the index-2 stationary point A (red dashed lines). The minimizer C is connected to B_1 and B_2 (yellow dashed lines). The surface color from blue to yellow represents energy from low to high.

example in Figure 1, we may implement the upward search algorithm by using 1-CHiSD from a minimizer C to obtain one of the index-1 saddle points B_1 and B_2. Then, the index-2 stationary point A is achieved from this index-1 saddle point by applying 2-CHiSD. A combination of the downward and upward search algorithms enables the entire search to navigate up and down on the solution landscape so that all of the excited states can be identified as long as they are connected somewhere.

RESULTS AND DISCUSSION

Winding numbers

To illustrate a vortex state ϕ, the particle density $|\phi|^2$ of each state is plotted in D within a common color bar. Quantized vortices locate at points where $|\phi|^2 = 0$ and can be further classified according to their winding numbers. The winding number (topological charge) is an important feature of a quantized vortex, defined as how many times of 2π that the argument of ϕ changes around this vortex. The ground state at $\Omega = 0$, denoted as O, has no vortices. To distinguish various vortex states, we denote "P" as a vortex of a winding number +1 and "N" as a -1 vortex. The number of multiple vortices is attached as subscripts. For example, P_2 represents two +1 vortices near the center. For multiply vortices (high winding numbers), we denote "P^m" as a $+m$ vortex.

Because of the trapping potential V, the majority of particle density lies inside a circle $\{\boldsymbol{x} \in \mathbb{R}^2 : \|\boldsymbol{x}\| = 4\}$, whereas vortices of some states locate outside nearby this circle. Therefore, we use "s" to separate vortices near the center and at the side. For example, P_2 has two +1 vortices near the center, and sP_2 has two +1 side vortices near the circle. NP_4 has a -1 central vortex with four +1 vortices surrounded nearby, whereas four +1 vortices of NsP_4 locate outside.

In the absence of rotation ($\Omega = 0$), both P and N exist as 2-saddles. With a positive frequency Ω, vortices with positive winding numbers will be energetically favorable compared to those with negative winding numbers.

Excitation mechanisms

Without loss of generality, we demonstrate that excited states of BECs possess a variety of vortex structures at two frequencies, $\Omega = 0.3$ and 0.45, as illustrations. Four excitation mechanisms are summarized by constructing solution landscapes.

Vortex addition. The first and very common excitation mechanism is the vortex addition (i.e., adding new vortices from the far field). As shown in the black solid arrows of Figure 2A, this mechanism can be commonly observed in the $\Omega = 0.3$ case, where P is the ground state and O is the first excited state. Adding a side vortex of winding number +1 to O leads to an excited state sP, and further, another excited state sP_2. From the perspective of rare events, sP is the transition state (1-saddle) connecting O and P, and the unstable direction of sP

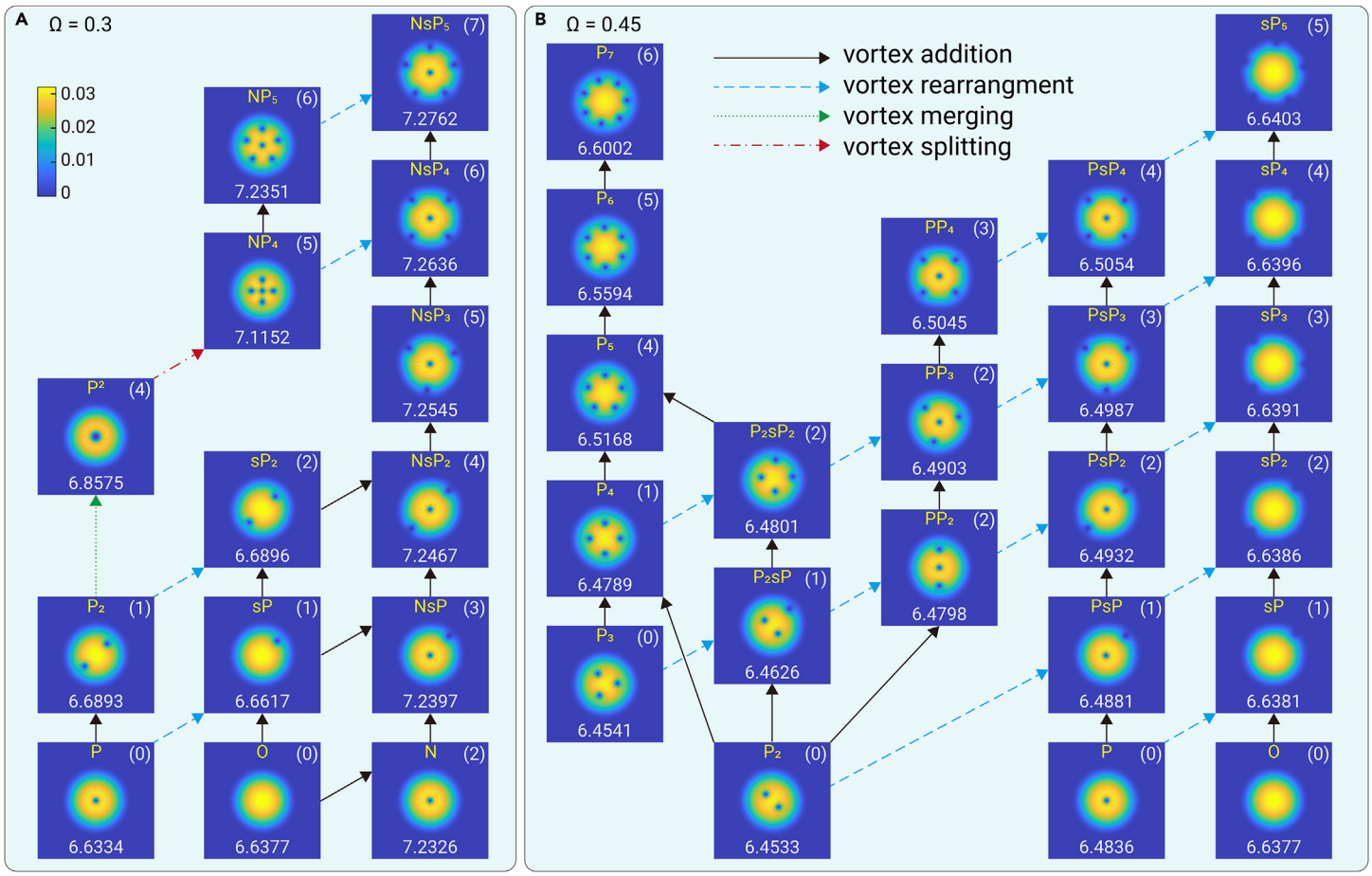

Figure 2. Excitation examples of four excitation mechanisms (A) $\Omega = 0.3$. (B) $\Omega = 0.45$. The four excitation mechanisms are vortex addition (black solid arrows), rearrangement (blue dashed arrows), merging (green dotted arrow), and splitting (red dot-dash arrow). For each state here and after, its particle density $|\phi|^2$ is plotted in D within a common color bar, and its name (top), energy (bottom), and index (top right parentheses) are labeled.

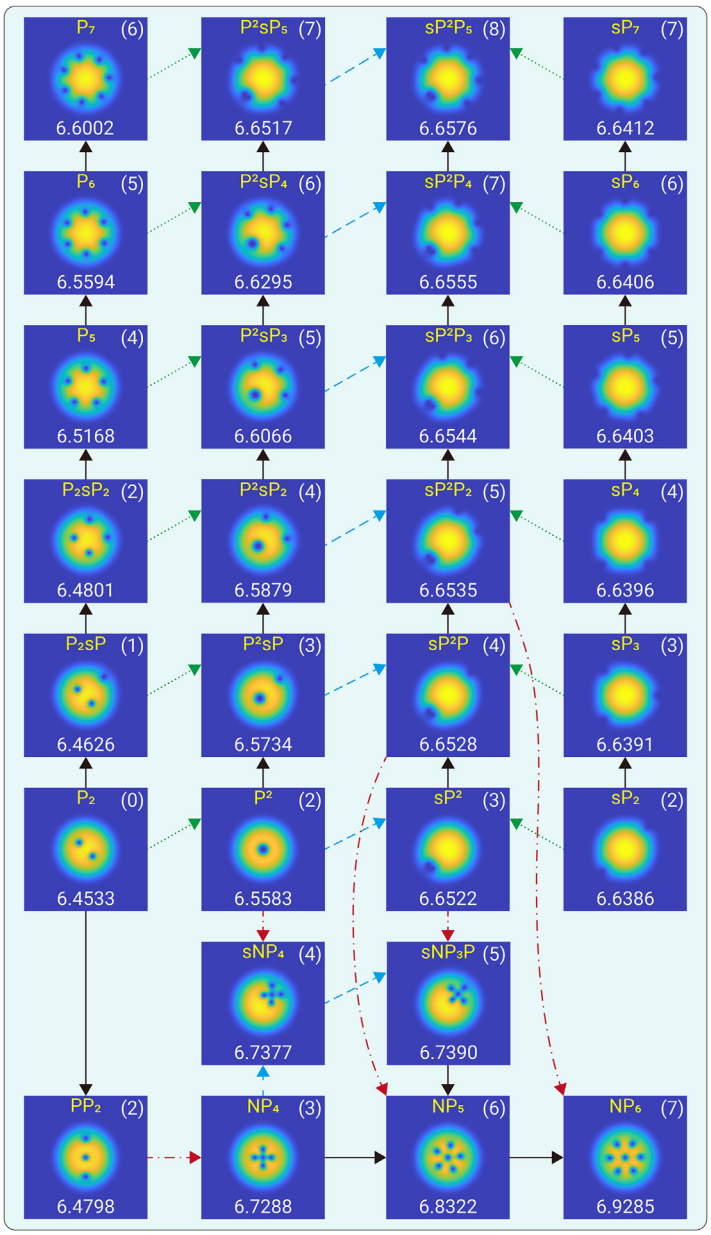

Figure 3. Excitation examples at $\Omega = 0.45$ The legends are the same as Figure 2.

corresponds to moving the vortex toward the center or outward. This vortex addition mechanism can also be found in the excitation sequence N → NsP → NsP_2 → NsP_3 → NsP_4 → NsP_5 (see Video S1). Along each excitation step, one +1 vortex is added from the far field to nearby the circle.

As shown in Figure 2B, more examples can be found at $\Omega = 0.45$, each of which involves an additional +1 vortex from the far field. In this case, P_2 and P_3 are the ground state and the first excited state, with similar energies. From P_2, we can add side vortices as P_2 → P_2sP → P_2sP_2. Once a side vortex is added, the index accordingly increases by one. We can also add vortices around the central vortex to obtain P_2 → PP_2 → PP_3 → PP_4. From P_3, we can successively add one middle vortex at a time to obtain excitations P_3 → P_4 → P_5 → P_6 → P_7, where vortices are arranged as regular polygons. Compared to a side vortex, adding a middle one often increases the energy more significantly. There are four local minimizers in this system, namely O, P, P_2, and P_3, connected by three transition states, sP, PsP, and P_2sP, each of which has exactly one side vortex. Along each minimum energy pathway, one +1 vortex is introduced from the far field to the middle. Note that P_2sP has also been obtained as the transition state between P_2 and P_3 in reference [42].

Vortex rearrangement. Because of the confining trap, vortex positions significantly affect the energy. At $\Omega = 0.3$, the ground state P can be excited to the transition state sP by moving the central +1 vortex outward. Similarly, NP_4 and NP_5 can also be excited to NsP_4 and NsP_5, respectively, by rearranging the +1 vortices outward simultaneously, as shown in the blue dashed arrows of Figure 2A.

At $\Omega = 0.45$, various vortex structures with the same number of vortices can be identified. For P_2 with two vortices, moving one outward and the other to the center leads to a 1-saddle PsP, while moving both leads to sP_2. For P_3 with three vortices, once a vortex is rearranged outside, the system is excited and the index increases by one. Three vortices can also be aligned compactly as a 2-saddle PP_2 with a lower value of the energy than PsP_2. Consequently, we obtain an excitation sequence P_3 → P_2sP → PP_2 → PsP_2 → sP_3 (see Video S2). Similar excitations also occur for states with more vortices such as P_4.

Vortex merging. The stationary states presented above only involve vortices with winding numbers ±1, whereas the BEC system also admits excited states with multiply vortices.[12] In fact, multiply vortices already exist in stationary states at $\Omega = 0$, such as a central vortex state P^2. Although one +2 vortex has the same winding number as two +1 vortices, this topological excitation often has a higher value of the energy and more unstable directions.[43] At $\Omega = 0.3$, merging two vortices of P_2 leads to P^2 with a significant energy increase, as shown in the green dotted arrow of Figure 2A. P^2 is a 4-saddle with four unstable directions, two of which move the vortex outward, and the other two split it into two +1 vortices.

At $\Omega = 0.45$, multiple states with +2 vortices can be obtained by merging. Merging two vortices of P_2 also leads to P^2, which is a 2-saddle (see Video S3). Along the unstable directions of P^2, the +2 vortex is split into two vortices, whereas moving the vortex outward leads to a 3-saddle sP^2, which can also be obtained by vortex merging from sP_2. We can also add side vortices successively to P^2, with the index increasing by one for each side vortex, as shown in the excitation sequence P^2 → P^2sP → P^2sP_2 → P^2sP_3 → P^2sP_4 → P^2sP_5, with the +2 vortex going farther from the center. These states can also be obtained by vortex merging from P_2sP, P_2sP_2, P_5, P_6, and P_7, respectively. Similarly, sP^2P_n ($n = 1, \ldots, 5$) can be obtained by the successive vortex addition of sP^2, merging of sP_{n+2}, or rearranging P^2sP_n. We enumerate these states in Figure 3, with multiple excitation relations started from P_2 and sP_2.

Vortex splitting. One vortex can also be split into multiple ±1 vortices as an excitation mechanism. At $\Omega = 0.3$, the +2 vortex of P^2 can be split into three +1 vortices and one −1 vortex. With an addition of a fourth +1 vortex from the far field, the system is excited to NP_4, as shown in the red dot-dash arrow of Figure 2A.

In the $\Omega = 0.45$ case, similar excitation pathways can be identified. From the 2-saddle P^2, the +2 vortex can also be split into three +1 vortices and one −1 vortex, leading to sNP_4 with an additional +1 vortex from the far field. In a similar manner of vortex splitting, sNP_3P, NP_5, and NP_6 can also be obtained from sP^2, sP^2P, and sP^2P_2, respectively. Although vortex splitting does not change the total winding number, the additional vortices in these examples above do. A +1 vortex can also be split into two +1 vortices and a −1 vortex, with the total winding number unchanged. From PP_2, the central vortex can split in this way and the system is excited to NP_4 (see Video S4), with no other vortices added.

Spectrum of stationary states

Four excitation mechanisms are summarized above to generate excited states with different vortex structures. Among these mechanisms, vortex addition will also change the total winding number. Various excited states can be obtained using these mechanisms, and the CHiSD method can uncover these excitation pathways.

Besides the excited states presented in Figures 2 and 3, we present the full spectrum of excited states found by the proposed method in Figures S2 ($\Omega = 0.3$) and S3 ($\Omega = 0.45$). A rich variety of vortex structures can be systematically obtained. As the rotational frequency increases, the system can accommodate more positive vortices. Note that theoretically an infinite number of excited states is expected in this system, so the upward search can be implemented continuously to obtain new excited states. The presented results are not the entire family of stationary states.

Because the ground state and excited states are discussed in terms of energy, the stationary states are sorted in the ascending order of energy. The chemical potential μ does not follow the same order, which is illustrated in Figure S4. The

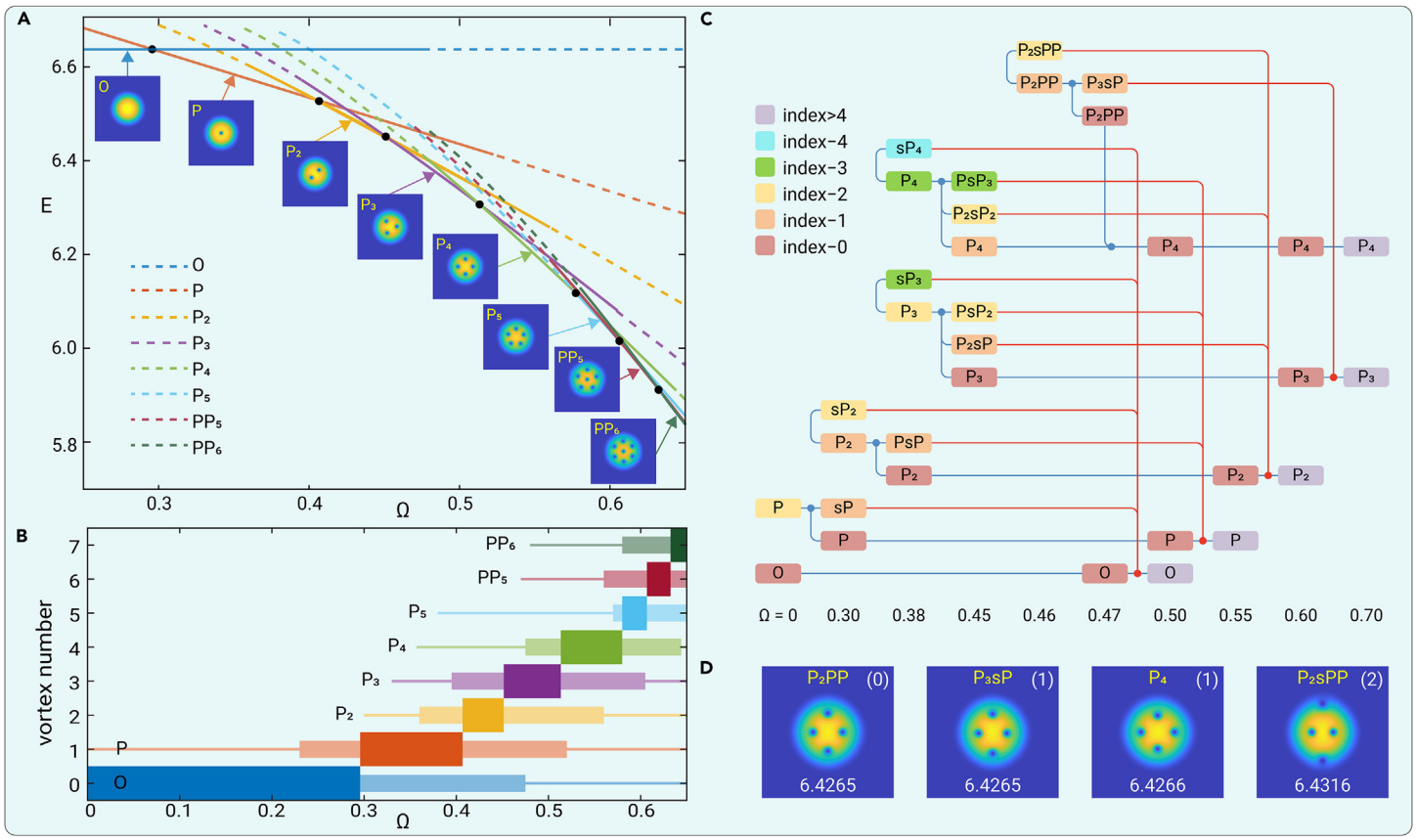

Figure 4. Diagrams of the stability of different states (A) An energy diagram for different Ω. As Ω increases, the ground state is, respectively, O, P, P_2, P_3, P_4, P_5, PP_5, and PP_6. Solid and dashed lines represent local minimizers and saddle points, respectively, and black dots indicate critical frequencies where the ground state changes. (B) The stability of each state. Solid rectangles indicate that the corresponding state is the ground state, and narrower light rectangles indicate that the corresponding state is a local minimizer and excited state. The solid line indicates where the state exists as a saddle point. (C) Bifurcation diagram of some stationary states. The color of each node represents its index. O and P exist at $\Omega = 0$, and P_2, P_3, P_4, and P_2PP emerge via saddle-node bifurcations. Solid lines denote solution branches, and T-junctions with dots denote pitchfork bifurcations. Blue lines represent solution branches maintaining vortices inside, and red lines represent that some vortices move to the far field as Ω increases. (D) Some states at $\Omega = 0.47$ involved in the stabilization of P_4.

stability based on the Morse index here is different from that of the Bogoliubov-de Gennes equation. The latter addresses the real-time stability about the stationary states of the time-dependent G-P equation.[3,11,44] Under the framework of the G-P energy and the CHiSD method, we can establish connections between different stationary states and calculate their transitions.

Phase diagram

As the rotational frequency Ω exceeds a critical frequency, quantum phase transition takes place and the ground state undergoes a topological change. As a result, the vortex structure of the ground state experiences successive topological changes with the increase in the frequency, as shown in the phase diagram in Figure 4A and the stability illustration for each state in Figure 4B. For each ground state, the average position of vortices is located at the origin. Similar vortex configurations and phase diagrams have also been reported in reference [12].

We start our discussion of the ground state evolution from O, the ground state at $\Omega = 0$. As Ω increases, O becomes a local minimizer (eg, the first excited state at $\Omega = 0.3$ and the 22nd excited state at 0.45) and then a saddle point, and its energy remains almost unchanged. The ground state at $\Omega = 0.3$ is P, which exists as a 2-saddle at $\Omega = 0$. After a pitchfork bifurcation, P becomes a local minimizer, with sP emerging as a 1-saddle. Because P is a central vortex state, its Hessian has only one zero eigenvalue, whereas the Hessian at sP has two zero eigenvalues. The different multiplicities of zero eigenvalues lead to index jumping of P. As Ω increases, the energy of P continues decreasing as plotted in Figure 4A, so that P replaces O as the ground state at the critical frequency.[12] Meanwhile, the 1-saddle sP moves its vortex far away and finally merges with O via a pitchfork bifurcation at $\Omega \approx 0.47$, which makes O an unstable saddle point.

At $\Omega = 0.45$, P_2 exists as the ground state. In fact, P_2 and sP_2 do not exist in the $\Omega = 0$ case, and emerge as saddle points via a saddle-node bifurcation at $\Omega < 0.3$. Then, P_2 becomes a local minimizer via a pitchfork bifurcation, generating a 1-saddle PsP. The two vortices of P_2 become closer, which accords with the results in the Thomas-Fermi regime.[12] Because P_2 has more positive vortices than P, the energy of P_2 decreases faster as Ω increases, and P_2 replaces P as the ground state, and P exists as an excited state and local minimizer. Meanwhile, the 1-saddle PsP moves its side vortex away and finally merges with P at $\Omega \approx 0.53$, which then makes P an unstable saddle point. As Ω increases, P goes through a sequence of "saddle point → local minimizer → global minimizer → local minimizer → saddle point," which exhibits as "excited state → ground state → excited state." As shown in Figure 4A, for a ground state at a higher frequency, which often accommodates more vortices, the energy decreases faster than the previous ground state with the increasing frequency. Consequently, the ground states changes successively and the number of the vortices in the ground state also increases. These results are qualitatively consistent with the theoretical predictions in the Thomas-Fermi regime.[11,12]

Bifurcation diagram

To clearly illustrate how the excited states become stabilized, a bifurcation diagram is presented in Figure 4C. The change in the stability property of P is very generic for ground states at other Ω, including P_2, P_3, and P_4. After emergence, these states become more stable via some pitchfork bifurcations, and at the same time, some saddle points with central and side vortices are generated. For each state after bifurcation, each side vortex near the circle brings an unstable direction, because moving it either outward or toward the center will decrease the energy, so its side vortex number coincides with its index. Finally, as Ω increases, the side vortices move to the far field (illustrated with red lines in Figure 4C), and the state merges with the corresponding local minimizer, leading to a high-index saddle point with central vortices.

The stabilization of P_4 is a little complicated because another state P_2PP is involved. P_2PP emerges as a 1-saddle first, and then is stabilized as a local minimizer via a pitchfork bifurcation, with a 1-saddle P_3sP emerging. For a larger Ω, P_4 is stabilized from a 1-saddle to a local minimizer via a pitchfork bifurcation involving this local minimizer P_2PP. We present these states at $\Omega = 0.47$ in Figure 4D to illustrate this stabilization.

For a larger Ω, the ground state would possess more vortices, and these vortices arrange themselves as multiple layers, as a result of the repulsive interactions between vortices and the attractive interactions between the vortices and the condensates. For example, at $\Omega = 0.62$ and 0.64, respectively, PP_5 and PP_6 have a lower energy than P_6 and P_7. For a fast-rotating condensate, the ground state can possess a complicated vortex lattice.[17,45] A regular vortex structure can appear in the ground state.

Conclusion

This study provides a comprehensive and systematic examination of the vortex states and the excitation mechanisms in rotational BECs trapped in an isotropic harmonic-oscillator potential. Using a solution landscape approach by the CHiSD method combined with downward/upward search algorithms, the excited states of 2D rotational BECs are revealed systematically. Four distinct excitation mechanisms are identified from the results: vortex addition, rearrangement, merging, and splitting. For each mechanism, we include a video to illustrate the vortex behavior. An excited state can be obtained along one or a few excitation pathways. The changes in the ground state with increasing rotational frequencies are depicted using an energy diagram and explained through a bifurcation diagram. As the rotational frequency increases, the ground state has more quantized vortices with a +1 winding number. We also show that the ground state at a high rotational frequency actually emerges as an excited state at a low frequency first and is then stabilized with the increase in the frequency. For an overlarge frequency, this state becomes an excited state again. The change in the stability property is generic for ground states at different frequencies.

The work can be naturally generalized to BECs trapped in an anisotropic harmonic-oscillator potential[13] to discover the corresponding excitation mechanisms. For example, in the isotropic scenario, vortex addition along any direction from one minimizer O to another P corresponds to an identical energy barrier. However, in an anisotropic scenario, vortex addition along different directions may result in different energy barriers, which could depend on the curvature of the anisotropic potential.

The methodology presented in this study offers an efficient numerical algorithm that constructs a complete solution landscape. It serves as a powerful tool for solving a wide range of quantum systems, including self-attractive BECs,[46] two-component BECs,[47] spinor BECs,[2,48] superconductors,[42,49] and fermionic wave functions.[50–52]

REFERENCES

1. Matthews, M.R., Anderson, B.P., Haljan, P.C., et al. (1999). Vortices in a Bose-Einstein condensate. Phys. Rev. Lett. ***83***, 2498–2501.
2. Kawaguchi, Y., and Ueda, M. (2012). Spinor Bose–Einstein condensates. Phys. Rep. ***520***, 253–381.
3. Dalfovo, F., Giorgini, S., Pitaevskii, L.P., et al. (1999). Theory of Bose-Einstein condensation in trapped gases. Rev. Mod. Phys. ***71***, 463–512.
4. Leggett, A.J. (2001). Bose-Einstein condensation in the alkali gases: Some fundamental concepts. Rev. Mod. Phys. ***73***, 307–358.
5. Cornell, E.A., and Wieman, C.E. (2002). Nobel lecture: Bose-Einstein condensation in a dilute gas, the first 70 years and some recent experiments. Rev. Mod. Phys. ***74***, 875–893.
6. Bao, W., and Cai, Y. (2013). Mathematical theory and numerical methods for Bose–Einstein condensation. Kinet. Relat. Models ***6***, 1–135.
7. Caradoc-Davies, B.M., Ballagh, R.J., and Burnett, K. (1999). Coherent dynamics of vortex formation in trapped Bose–Einstein condensates. Phys. Rev. Lett. ***83***, 895–898.
8. Madison, K.W., Chevy, F., Wohlleben, W., et al. (2000). Vortex formation in a stirred Bose–Einstein condensate. Phys. Rev. Lett. ***84***, 806–809.
9. Abo-Shaeer, J.R., Raman, C., Vogels, J.M., et al. (2001). Observation of vortex lattices in Bose–Einstein condensates. Science ***292***, 476–479.
10. Coddington, I., Engels, P., Schweikhard, V., et al. (2003). Observation of Tkachenko oscillations in rapidly rotating Bose-Einstein condensates. Phys. Rev. Lett. ***91***, 100402.
11. Fetter, A.L. (2009). Rotating trapped Bose-Einstein condensates. Rev. Mod. Phys. ***81***, 647–691.
12. Aftalion, A., and Du, Q. (2001). Vortices in a rotating Bose-Einstein condensate: Critical angular velocities and energy diagrams in the Thomas-Fermi regime. Phys. Rev. A ***64***, 063603.
13. Bao, W., Wang, H., and Markowich, P.A. (2005). Ground, symmetric and central vortex states in rotating Bose–Einstein condensates. Comm. Math. Sci. ***3***, 57–88.
14. Cai, Y., Yuan, Y., Rosenkranz, M., et al. (2018). Vortex patterns and the critical rotational frequency in rotating dipolar Bose-Einstein condensates. Phys. Rev. A ***98***, 023610.
15. Milnor, J. (1963). Morse Theory (Princeton University Press).
16. Butts, D.A., and Rokhsar, D.S. (1999). Predicted signatures of rotating Bose–Einstein condensates. Nature ***397***, 327–329.
17. Aftalion, A., Blanc, X., and Dalibard, J. (2005). Vortex patterns in a fast rotating Bose-Einstein condensate. Phys. Rev. A ***71***, 023611.
18. Bao, W., and Du, Q. (2004). Computing the ground state solution of Bose–Einstein condensates by a normalized gradient flow. SIAM J. Sci. Comput. ***25***, 1674–1697.
19. Bao, W., Chern, I.L., and Lim, F.Y. (2006). Efficient and spectrally accurate numerical methods for computing ground and first excited states in Bose–Einstein condensates. J. Comput. Phys. ***219***, 836–854.
20. Edmonds, M., and Nitta, M. (2020). Vortex patterns of atomic Bose-Einstein condensates in a density-dependent gauge potential. Phys. Rev. A ***102***, 011303.
21. Takeuchi, H. (2021). Quantum elliptic vortex in a nematic-spin Bose-Einstein condensate. Phys. Rev. Lett. ***126***, 195302.
22. Kasamatsu, K., Tsubota, M., and Ueda, M. (2003). Nonlinear dynamics of vortex lattice formation in a rotating Bose-Einstein condensate. Phys. Rev. A ***67***, 033610.
23. Weiler, C.N., Neely, T.W., Scherer, D.R., et al. (2008). Spontaneous vortices in the formation of Bose–Einstein condensates. Nature ***455***, 948–951.
24. Law, K.J.H., Kevrekidis, P.G., and Tuckerman, L.S. (2010). Stable vortex–bright-soliton structures in two-component Bose–Einstein condensates. Phys. Rev. Lett. ***105***, 160405.
25. Law, K.J.H., Neely, T.W., Kevrekidis, P.G., et al. (2014). Dynamic and energetic stabilization of persistent currents in Bose–Einstein condensates. Phys. Rev. A ***89***, 053606.
26. Charalampidis, E.G., Kevrekidis, P.G., and Farrell, P.E. (2018). Computing stationary solutions of the two-dimensional Gross–Pitaevskii equation with deflated continuation. Commun. Nonlinear Sci. Numer. Simul. ***54***, 482–499.
27. Raman, C., Abo-Shaeer, J.R., Vogels, J.M., et al. (2001). Vortex nucleation in a stirred Bose-Einstein condensate. Phys. Rev. Lett. ***87***, 210402.
28. Madison, K.W., Chevy, F., Bretin, V., et al. (2001). Stationary states of a rotating Bose-Einstein condensate: Routes to vortex nucleation. Phys. Rev. Lett. ***86***, 4443.
29. Price, R.M., Trypogeorgos, D., Campbell, D.L., et al. (2016). Vortex nucleation in a Bose–Einstein condensate: from the inside out. New J. Phys. ***18***, 113009.
30. Yin, J., Wang, Y., Chen, J.Z.Y., et al. (2020). Construction of a pathway map on a complicated energy landscape. Phys. Rev. Lett. ***124***, 090601.
31. Yin, J., Yu, B., and Zhang, L. (2021). Searching the solution landscape by generalized high-index saddle dynamics. Sci. China Math. ***64***, 1801–1816.
32. Han, Y., Yin, J., Hu, Y., et al. (2021). Solution landscapes of the simplified Ericksen–Leslie model and its comparison with the reduced Landau–de Gennes model. Proc. R. Soc. A ***477***, 20210458.
33. Shi, B., Han, Y., and Zhang, L. (2022). Nematic liquid crystals in a rectangular confinement: Solution landscape, and bifurcation. SIAM J. Appl. Math. ***82***, 1808–1828.
34. Wang, W., Zhang, L., and Zhang, P. (2021). Modelling and computation of liquid crystals. Acta Numer. ***30***, 765–851.
35. Yin, J., Zhang, L., and Zhang, P. (2022). Solution landscape of the Onsager model identifies non-axisymmetric critical points. Physica D ***430***, 133081.
36. Yin, J., Jiang, K., Shi, A.C., et al. (2021). Transition pathways connecting crystals and quasicrystals. Proc. Natl. Acad. Sci. USA ***118***, e2106230118.
37. Xu, Z., Han, Y., Yin, J., et al. (2021). Solution landscapes of the diblock copolymer-homopolymer model under two-dimensional confinement. Phys. Rev. E ***104***, 014505.
38. Knyazev, A.V. (2001). Toward the optimal preconditioned eigensolver: Locally optimal block preconditioned conjugate gradient method. SIAM J. Sci. Comput. ***23***, 517–541.
39. Yin, J., Huang, Z., and Zhang, L. (2022). Constrained high-index saddle dynamics for the solution landscape with equality constraints. J. Sci. Comput. ***91***, 62.
40. Zhang, L., Zhang, P., and Zheng, X. (2023). Discretization and index-robust error analysis for constrained high-index saddle dynamics on the high-dimensional sphere. Sci. China Math. ***66***, 2347–2360.
41. Absil, P.A., Mahony, R., and Sepulchre, R. (2008). Optimization Algorithms on Matrix Manifolds (Princeton University Press).
42. Schweigert, V.A., and Peeters, F.M. (1999). Flux penetration and expulsion in thin superconducting disks. Phys. Rev. Lett. ***83***, 2409–2412.
43. Kasamastu, K., and Tsubota, M. (2009). Quantised vortices in atomic Bose–Einsten condensates. Prog. Low Temp. Phys. ***16***, 351–403.
44. Gao, Y., and Cai, Y. (2020). Numerical methods for Bogoliubov-de Gennes excitations of Bose-Einstein condensates. J. Comput. Phys. ***403***, 109058.
45. Aftalion, A., and Blanc, X. (2006). Vortex lattices in rotating Bose–Einstein condensates. SIAM J. Math. Anal. ***38***, 874–893.
46. Mihalache, D., Mazilu, D., Malomed, B.A., et al. (2006). Vortex stability in nearly-two-dimensional Bose-Einstein condensates with attraction. Phys. Rev. A ***73***, 043615.
47. Hammond, A., Lavoine, L., and Bourdel, T. (2022). Tunable three-body interactions in driven two-component bose-einstein condensates. Phys. Rev. Lett. ***128***, 083401.
48. Chai, X., Lao, D., Fujimoto, K., et al. (2020). Magnetic solitons in a spin-1 Bose-Einstein condensate. Phys. Rev. Lett. ***125***, 030402.

49. Benfenati, A., Maiani, A., Rybakov, F.N., et al. (2020). Vortex nucleation barrier in superconductors beyond the Bean-Livingston approximation: A numerical approach for the sphaleron problem in a gauge theory. Phys. Rev. B ***101***, 220505.
50. Zhang, J.M., and Kollar, M. (2014). Optimal multiconfiguration approximation of an *n*-fermion wave function. Phys. Rev. A ***89***, 012504.
51. Zhang, J.M., and Mauser, N.J. (2016). Optimal Slater-determinant approximation of fermionic wave functions. Phys. Rev. A ***94***, 032513.
52. Aoto, Y.A., and da Silva, M.F. (2020). Calculating the distance from an electronic wave function to the manifold of Slater determinants through the geometry of Grassmannians. Phys. Rev. A ***102***, 052803.

ACKNOWLEDGMENTS

We thank Prof. Weizhu Bao and Prof. Biao Wu for the helpful discussions. L.Z. is supported by the National Key Research and Development Program of China 2021YFF1200500 and the National Natural Science Foundation of China (No. 12225102, T2321001, 12050002, and 12288101). J.Y. is supported by the National Research Foundation, Singapore (Project No. NRF-NRFF13-2021-0005). Q.D. is supported by the National Science Foundation (DMS-2012562 and DMS-1937254). Y.C. is supported by the National Natural Science Foundation of China (No. 12171041).

AUTHOR CONTRIBUTIONS

L.Z. and Y.C. designed the research; J.Y. and Z.H. performed the research; J.Y., Z.H., Y.C., Q.D., and L.Z. analyzed the results; J.Y. and L.Z. wrote the paper; Y.C., Q.D., and L.Z. participated in manuscript revision.

DECLARATION OF INTERESTS

The authors declare no competing interests.

SUPPLEMENTAL INFORMATION

It can be found online at https://doi.org/10.1016/j.xinn.2023.100546.

LEAD CONTACT WEBSITE

http://faculty.bicmr.pku.edu.cn/~zhanglei/.